JOURNAL OF COMPUTATIONAL PHYSICS 113, 165–176 (1994)

A "Stratified" Spectral Model for Stable and Convective Atmospheres

KWING L. CHAN

Applied Research Corporation, Landover, Maryland 20785

H. G. MAYR

NASA/Goddard Space Flight Center, Greenbelt, Maryland 20771

J. G. MENGEL

Applied Research Corporation, Landover, Maryland 20785

AND

I. HARRIS

NASA/Goddard Space Flight Center, Greenbelt, Maryland 20771

Received June 16, 1992; revised October 28, 1993

In our solar system, convective atmospheres are as common as those that are stable, and convective and stable regions sometimes coexist in the same atmosphere. There is a need to develop circulation models that can handle convection and stable-layer flows simultaneously and efficiently. This paper represents an approach to the construction of such a model. Taking advantages of the simplicity of implementing implicit time stepping in spectral models, we solve a non-hydrostatic, fully compressible version of the hydrodynamic equations without the time step restrictions imposed by acoustic and gravity waves. To simplify the nonlinear terms and to conserve the total mass and total angular momentum to round-off accuracy, we introduce a "stratified" approximation which limits the nonlinearity of the equations to quadratic. The linear terms remain intact so that all the linear waves are preserved. The set of assumptions made by the "stratified" approximation is a subset of those of the anelastic approximation. It offers more generality and accuracy while the computational overhead is relatively low. Tests are presented to illustrate the capabilities and advantages of the present model.

1. INTRODUCTION

The study of nonlinear hydrodynamic processes in atmospheres requires numerical computations. This is true for the simulation or prediction of weather in the Earth's atmosphere. It is also true for the study of planetary and solar atmospheres, and for identifying the key hydrodynamic factors that control atmospheric behavior in general. A few examples of the fundamental questions being asked are: What generates the global zonal wind that moves the Venusian clouds at a rate 60 times faster than the rotation rate of the planet [1]? Is there a common explanation for the alternating zonal winds of Jupiter, Saturn, Neptune, and the Sun [2–5]? Why are the magnitudes of these zonal winds insensitive to the planet's distance from the Sun [6]? What causes the failure of the Taylor–Proudman theorem in the solar convection zone [7, 8]? These questions involve the comparative study of a wide variety of atmospheres.

Current general circulation models (GCM) of the Earth's atmosphere are often not well suited to address the above problems, since some of the elaborate parameterizations they carry are not always desirable or applicable. Furthermore, these GCMs are not designed to study the convective atmospheres of the outer planets and the Sun. Some problems are numerically so demanding that direct simulations are not practical, and numerical experiments serve better for uncovering the dynamical principles [9]. For comparative studies, there is a need, therefore, to develop a simpler, efficient, and general-purpose code capable of modeling circulations in convective and stable atmospheres. This paper describes an approach to the construction of such a model. We present here a spectral model that solves a non-hydrostatic, "stratified" version (see Section 2) of the compressible Navier–Stokes equations.

Soon after the development of the transform method by Orszag [10] and Eliasen *et al.* [11], the spectral approach to atmospheric modeling [12–15] became an important

0021-9991/94 $6.00

tool in the field of general circulation study [16–21]. Compared to finite-difference models, the spectral transform models have several advantages: (i) the polar regions can be handled naturally and efficiently; (ii) at low to moderate horizontal resolutions, they are computationally more efficient [22–23]; (iii) semi-implicit time differencing schemes [24–25] can be easily implemented. It is the last point that is exploited in developing our model scheme.

Many convective atmospheres are deep, and the vertical and horizontal length scales are comparable. For this reason the long-wave approximation, and equivalently, the hydrostatic approximation, are not applicable. Solving the Navier–Stokes equations directly, however, is numerically expensive because of the restrictive Courant–Friedrichs–Lewy (CFL) condition imposed on the time steps by the sound waves; i.e., the time steps have to be less than the signal crossing time of any two adjacent grid points. To overcome this problem, the non-hydrostatic, anelastic form of the Navier–Stokes equations [26–30] is often used. By setting the local time derivative of the mass continuity equation to zero, the anelastic approximation eliminates sound waves and the associated restriction. The CFL condition associated with the flow speed remains, but it is less restrictive if the fluid velocities are substantially smaller than the sound speed, as is usually the case in normal atmospheres.

There is an alternative which avoids modifying the continuity equation. The restrictive CFL condition due to the waves only affects the numerical stability of explicit time-differencing methods. The restriction can be avoided by methods that handle the linear wave terms implicitly [24, 31–32]. With the spectral method used in the present model, this is rather straightforward. However, to optimize the conservation of the integrals of motion and to eliminate aliasing errors, it is necessary to introduce approximations and to reformulate the equations carefully. We discuss this subject in the next section. Then, we discuss the numerical implementation of the model in Section 3. Several tests to illustrate the characteristics of the model are present in Section 4. A summary is provided in Section 5. In the Appendix, we expand on contrasting the present approach with the anelastic approach and discuss the relative significance of the time derivative term in the continuity equation, based on an example computed by solving the fully compressible Navier–Stokes equations.

2. THE STRATIFIED APPROXIMATION

As stated above, the linear terms will be treated implicitly; thus, there is no need to tamper with them. For the nonlinear terms, we introduce a "stratified approximation" which restricts the terms to be quadratic in the spectral multiplication, so that the transforms can be alias-free without the use of too many grid points. This helps to enforce the conservation of certain integrals of motion (e.g., total mass and total angular momentum) which, aside from making the system dynamically more correct, may also enhance the numerical stability [33–34].

For an incompressible fluid, the nonlinearities are only quadratic. In a compressible fluid, higher degrees of nonlinearity are introduced through the variation of density in the momentum equation and the variation of the thermodynamic variables in the energy equation. Under normal atmospheric conditions (even for deep, convecting atmospheres [35]), the distributions of the thermodynamic variables (excluding the entropy or the potential temperature) are dominated by the stratification; namely, at any given height the horizontal variations are small compared to the mean values. Each thermodynamic variable can be decomposed into two parts of widely different magnitudes; as an example, the density is shown here as

$$\rho(r, \theta, \phi, t) = \rho_0(r, t) + \rho_1(r, \theta, \phi, t). \tag{1}$$

The variables are expressed in standard spherical coordinate notations, where r is the radial distance, θ is the colatitudinal angle with respect to the north pole, and ϕ is the azimuthal angle. The subscripts 0 and 1 denote the horizontal average and the horizontal variation, respectively. After the substitution of such expansions in the fundamental hydrodynamic equations, the following approximations are made:

(i) in the momentum equation, the horizontal variation of the density is ignored in the nonlinear advection terms and the viscous terms.

(ii) in the energy equation, terms containing products of two or more horizontal variations of the thermodynamic variables are ignored.

These approximations are equivalent to a subset of the anelastic approximation. One can arrive at this procedure through a scale analysis leading to the anelastic equations [28], with the exception that the linear terms are retained to all orders of the perturbation expansion and no simplifying assumption is required for the temporal variations. This leaves the linear waves intact and offers a more consistent treatment of the density variation.

First, the fundamental hydrodynamic equations are expressed in the following form:

$$\partial_t \rho = -\nabla \cdot \mathbf{M} \tag{2}$$

$$\partial_t \mathbf{M} = -\nabla \cdot (\mathbf{M}\mathbf{M}/\rho) + \nabla \cdot \boldsymbol{\sigma} - \nabla p - 2\boldsymbol{\Omega} \times \mathbf{M} + \rho \mathbf{g} - \rho \boldsymbol{\Omega} \times (\boldsymbol{\Omega} \times \mathbf{r}) \tag{3}$$

$$\partial_t p = -\nabla \cdot (p\mathbf{M}/\rho) - (\Gamma - 1)\, p \nabla \cdot (\mathbf{M}/\rho) - \nabla_{\mathrm{ad}} \Gamma (\nabla \cdot \mathbf{f} - \varepsilon), \tag{4}$$

where $\mathbf{M}=\rho\mathbf{V}$ is the momentum density, $\mathbf{V}$ is the velocity, ρ is density, p is the pressure, $\mathbf{\Omega}$ is the angular velocity of the reference system, $\mathbf{g}$ is the gravitational acceleration, $\boldsymbol{\sigma}$ is the viscous stress tensor, Γ is the adiabatic exponent defined by $(d\ln p/d\ln\rho)_{ad}$, $\nabla_{ad}=(d\ln T/d\ln p)_{ad}$ is the adiabatic temperature gradient (see Chap. 9 of [36]), $\mathbf{f}$ is the radiative or conductive energy flux, and ε is a heating rate per unit volume (including the viscous dissipation of the kinetic energy). The bold-typed symbols represent vectors or tensors. The energy equation has been converted to the pressure equation (4) for the convenience of time-implicit treatment (note the linear dependence on p in Eq. (3)). For an ideal gas, Γ is equal to the ratio of specific heats γ, and ∇_{ad} is equal to $(\gamma-1)/\gamma$.

As in most spectral models, we use the vorticity and divergence instead of the horizontal velocities as prognostic variables. The equations for these variables are obtained by taking the horizontal curl and divergence of the momentum equation (3). Following general practice, the centrifugal potential (in the last term of (3)) can be combined with the gravitational potential and the deviation of the equipotential surfaces from perfect spheres are neglected. For simplicity, topography is not considered. After applying the stratified approximation and with some manipulation, one can reduce the hydrodynamic equations to

$$\partial_t\rho=-\mathscr{D}_{r2}M_r-\delta \tag{5}$$

$$\partial_t M_r=-\partial_r p-\rho g+C_r+D_r+N_r \tag{6}$$

$$\partial_t\delta=-\nabla_{\mathrm{H}}^2 p+C_\delta+D_\delta+N_\delta \tag{7}$$

$$\partial_t\zeta=+C_\zeta+D_\zeta+N_\zeta \tag{8}$$

$$\partial_t p=-\mathscr{D}_{r2}(p_0M_r/\rho_0)-(\Gamma_0-1)\,p_0\mathscr{D}_{r2}(M_r/\rho_0)-\Gamma_0 p_0\delta/\rho_0+D_p+N_p, \tag{9}$$

where ∂_r is the partial derivative with respect to r; $\mathscr{D}_{r2}(\ )=r^{-2}\partial_r r^2(\ )$; M_r is the radial component of $\mathbf{M}$; ∇_{H}^2 is the horizontal Laplacian $(rs)^{-2}(s\partial_\theta s\partial_\theta+\partial_\phi^2)$; s stands for $\sin\theta$; $\delta=\nabla_{\mathrm{H}}\cdot\mathbf{M}_{\mathrm{H}}=(rs)^{-1}(\partial_\theta sM_\theta+\partial_\phi M_\phi)$ is the horizontal divergence of the horizontal momentum density $\mathbf{M}_{\mathrm{H}}$; $\zeta=(\nabla_{\mathrm{H}}\times\mathbf{M}_{\mathrm{H}})_r=(rs)^{-1}(\partial_\theta sM_\phi-\partial_\phi M_\theta)$ is the curl of $\mathbf{M}_{\mathrm{H}}$ along the radial direction. The subscripts r and H denote components along the radial and horizontal directions, respectively. For convenience, the subscript r is dropped from the operator $(\nabla_{\mathrm{H}})_r$ hereafter; it is to be understood that the result of this operator is a single component quantity (a scalar).

The linear terms preceding the "C" terms in Eqs. (5)–(9) contain the description of acoustic and gravity waves; for later reference, we shall identify them as the W terms. The Coriolis terms are represented by the symbol C:

$$C_r=2\Omega sM_\phi \tag{10}$$

$$C_\delta=2\Omega[\chi\zeta-r^{-1}(sM_\phi+\partial_\phi M_r)] \tag{11}$$

$$C_\zeta=-2\Omega[\chi\delta-r^{-1}(sM_\theta-s\partial_\theta M_r-2\chi M_r)], \tag{12}$$

where χ stands for $\cos\theta$. The dissipative terms are:

$$D_r=2\mathscr{D}_{r2}(\mu_r\partial_r V_r)+\mu_{\mathrm{H}}\nabla_{\mathrm{H}}^2V_r+\mu_r\partial_r\delta_V-2\mu_{\mathrm{H}}r^{-1}(\delta_V+2r^{-1}V_r)+\partial_r[\lambda(\mathscr{D}_{r2}V_r+\delta_V)] \tag{13}$$

$$D_\delta=\mathscr{D}_{r4}(\mu_r\partial_r\delta_V+\mu_{\mathrm{H}}\nabla_{\mathrm{H}}^2V_r)+2\mu_{\mathrm{H}}(r^{-1}\nabla_{\mathrm{H}}^2V_r+\nabla_{\mathrm{H}}^2\delta_V+r^{-2}\delta_V)+\lambda[\mathscr{D}_{r4}(\nabla_{\mathrm{H}}^2V_r)+\nabla_{\mathrm{H}}^2\delta_V] \tag{14}$$

$$D_\zeta=\mathscr{D}_{r4}(\mu_r\partial_r\zeta_V)+\mu_{\mathrm{H}}(\nabla_{\mathrm{H}}^2\zeta_V+2r^{-2}\zeta_V) \tag{15}$$

$$D_p=\nabla_{ad}\Gamma[\mathscr{D}_{r2}(\kappa_{pr}\partial_r p+\kappa_{\rho r}\partial_r\rho)+\kappa_{p\mathrm{H}}\nabla_{\mathrm{H}}^2p+\kappa_{\rho\mathrm{H}}\nabla_{\mathrm{H}}^2\rho], \tag{16}$$

where $\delta_V=\nabla_{\mathrm{H}}\cdot\mathbf{V}_{\mathrm{H}}$; $\zeta_V=\nabla_{\mathrm{H}}\times\mathbf{V}_{\mathrm{H}}$, and $\mathscr{D}_{r4}(\ )=r^{-4}\partial_r r^4(\ )$. In the derivation of Eqs. (13)–(15), all the viscosity coefficients are assumed to have no horizontal variations. The radial and horizontal viscosities, μ_r and μ_{H}, are not necessarily equal here so that anisotropic eddy diffusion may be emulated. λ is the second coefficient of viscosity. When μ_r and μ_{H} are equal, the expressions are equivalent to those of the Navier–Stokes equations.

These viscous terms have two important characteristics. First, they preserve the solid body rotation as a stress-free state. A solid body rotation with an arbitrary angular velocity α yields $V_r=0$, $\delta_V=0$, and $\zeta_V=\chi\alpha$. These values make the right-hand sides (r.h.s.) of Eqs.(13)–(15) vanish. Second, they conserve the total angular momentum (relative to the reference frame) when the boundaries are spherical and stress-free (both $\partial_r\delta_V$ and $\partial_r\zeta_V$ are zero at the boundaries), as is demonstrated in the following. Consider the component of the total relative angular momentum along the axial direction; it can be written as

$$\int M_\phi rs\,d\varpi\,r^2\,dr=-\int(M_\phi\partial_\theta\chi-s^{-1}M_\theta\partial_\phi\chi)\,d\varpi\,r^3\,dr=\int\chi(rs)^{-1}(\partial_\theta sM_\phi-\partial_\phi M_\theta)\,d\varpi\,r^4\,dr=\int\chi\zeta\,d\varpi\,r^4\,dr, \tag{17}$$

where $d\varpi=s\,d\theta\,d\phi$ is an area element on the unit sphere. The rate of change of this integral due to viscous action then vanishes:

$$\int\chi\partial_r\zeta\,d\varpi\,r^4\,dr=-\int\partial_r(r^4\mu_r\partial_r\zeta_V)\,dr\,d\varpi+\int\mu_{\mathrm{H}}(\nabla_{\mathrm{H}}^2\zeta_V+2r^{-2}\zeta_V)\,d\varpi\,r^4\,dr=\int[s^{-1}\partial_\theta(s\partial_\theta\zeta_V)+2\zeta_V]\,d\varpi\,\mu_{\mathrm{H}}r^2\,dr=0. \tag{18}$$

Generally, the coefficients of viscosity are small, the ratios $\rho_0^{-1}M_r$, $\rho_0^{-1}\delta$, and $\rho_0^{-1}\zeta$ can be used as approximations for V_r, δ_V, and ζ_V, respectively. This converts Eqs. (13)–(15) to be linear in the prognostic variables, enabling them also to be treated implicitly.

In the derivation of (16), the energy flux is modeled as the negative gradient of a certain thermodynamic variable which is a function of ρ and p; the radial and horizontal conductivities (κ) are again allowed to be different. If $\mathbf{f} = -\kappa\nabla T$ (flux is proportional to the negative gradient of the temperature T) and the gas is ideal, it follows that $\kappa_p = \kappa\rho^{-1}$ and $\kappa_\rho = -\kappa p\rho^{-2}$. The horizontal fluctuations of the factor $(\nabla_{ad}\Gamma)$ and the conductivities can be taken to be small and expanded in forms similar to Eq. (1). The zeroth and first-order parts of the flux terms can be treated implicitly; the higher order parts can be treated explicitly or discarded.

Finally, the nonlinear terms are

$$N_r = -\mathscr{D}_{r2}(M_r V_r) - \nabla_H\cdot(M_r\mathbf{V}_H) + r^{-1}M_H V_H \tag{19}$$

$$N_\delta = -\mathscr{D}_{r4}[\nabla_H\cdot(M_r\mathbf{V}_H)] + \nabla_H\times(\zeta\mathbf{V}_H) - \nabla_H\cdot(\delta\mathbf{V}_H) - \nabla_H^2(M_H V_H)/2 \tag{20}$$

$$N_\zeta = -\mathscr{D}_{r4}[\nabla_H\times(M_r\mathbf{V}_H)] - \nabla_H\cdot(\zeta\mathbf{V}_H) - \nabla_H\times(\delta\mathbf{V}_H) \tag{21}$$

$$N_p = -\nabla\cdot(p_1\mathbf{V}) - (\Gamma_0 - 1)\,p_1\nabla\cdot\mathbf{V} + \nabla\cdot(p_0\rho_1\mathbf{V}/\rho_0) + (\Gamma_0 - 1)\,p_0\nabla\cdot(\rho_1\mathbf{V}/\rho_0) - \Gamma_1 p_0\nabla\cdot\mathbf{V} + \nabla_{ad}\Gamma\varepsilon. \tag{22}$$

The terms are arranged with the horizonal derivatives operating on the nonlinear products of the variables so that the number of transformations between the grid space and the spectral space can be reduced; especially, there is no need to transform derivatives of the prognostic variables. In accordance with the stratified approximation, the velocity $\mathbf{V}$ is approximated by $\mathbf{M}/\rho_0$.

In (22), the heating function ε includes the dissipation function:

$$\begin{aligned}\Phi = 2\{&\mu_r(\partial_r V_r)^2 + \mu_H r^{-2}[(\partial_\theta V_\theta + V_r)^2 \\ &+ (s^{-1}\partial_\phi V_\phi + V_r + V_\theta\cot\theta)^2]\} \\ &+ \mu_H[(rs)^{-1}\partial_\phi V_\theta + r^{-1}s\partial_\theta(V_\phi/s)]^2 \\ &+ [\mu_H(rs)^{-1}\partial_\phi V_r + \mu_r r\partial_r(V_\phi/r)] \\ &\times[(rs)^{-1}\partial_\phi V_r + r\partial_r(V_\phi/r)] \\ &+ [\mu_r r\partial_r(V_\theta/r) + \mu_H r^{-1}\partial_\theta V_r] \\ &\times[r\partial_r(V_\theta/r) + r^{-1}\partial_\theta V_r] + \lambda(\nabla\cdot\mathbf{V})^2.\end{aligned} \tag{23}$$

Again, when μ_r and μ_H are equal, Φ reduces to the dissipation function of the Navier–Stokes equations. When they are not equal, however, Φ is not positive definite, although it only turns negative under very contrived conditions. To keep the number of spectral transforms low, the velocity derivatives in Eq. (23) are computed by finite-difference in the grid space (with three-point Lagrangian interpolations).

An important property of the nonlinear terms above is the conservation of the total angular momentum when there is no external exchange. Similar to Eq. (18), the contribution of the nonlinear interaction to the rate of change of the total angular momentum along the axial direction can be shown to vanish:

$$\begin{aligned}\int \chi\partial_r\zeta\, d\varpi\, r^4\, dr &= -\int \partial_r[r^4\nabla_H\times(M_r\mathbf{V}_H)]\, dr\, d\varpi \\ &\quad + \int s(M_\theta\zeta + M_\phi\delta)\, d\varpi\, \rho_0^{-1}r^3\, dr \\ &= \int [sM_\theta\partial_\theta(sM_\phi) + sM_\phi\partial_\theta(sM_\theta)] \\ &\quad \times d\theta\, d\phi\, \rho_0^{-1}r^2\, dr = 0.\end{aligned} \tag{24}$$

The first term on the r.h.s. of the first equal sign vanishes because $M_r = 0$ at the inner and outer boundaries, and the other term vanishes because its integrand is a differential of θ. However, note that the C terms can change the total relative angular momentum if $\Omega \neq 0$.

The conservation of total mass can easily be proven by Eq. (5).

3. NUMERICAL METHODS

All the prognostic variables are scalars and therefore their horizontal dependencies can be represented by expansions in terms of the spherical harmonics. For example, the density can be written as

$$\rho = \sum \rho_n^m(r)\, P_n^m(\chi)\, e^{im\phi} \tag{25}$$

where P_n^m are the *normalized* associated Legendre functions. The triangular truncation is normally adopted for the series expansion, but in axisymmetric cases m is limited to zero. The horizontal mean ρ_0 in (1) is equal to $2^{-1/2}\rho_0^0$.

The linear terms of Eqs. (5)–(9) can be evaluated in spectral space. They are expressed in terms of the prognostic variables so that an implicit treatment can be implemented. The only horizontal differential operator in the W and D terms is ∇_H^2 which can be easily evaluated since $\nabla_H^2 P_n^m(\chi)\, e^{im\phi} = -n(n+1)\, P_n^m(\chi)\, e^{im\phi}$. By applying standard formulas for Legendre functions, the C terms can be put in the form

$$C_{rn}^m = 2\Omega r\{-c(n, m)\,\zeta_{n-1}^m + c(n+1, m)\,\zeta_{n+1}^m - im[n(n+1)]^{-1}\delta_n^m\} \tag{26}$$

$$C^m_{\delta n} = 2\Omega\{(n+1)\,c(n,m)\,\zeta^m_{n-1} + nc(n+1,m)\,\zeta^m_{n+1} + im[n(n+1)]^{-1}\,\delta^m_n - imM^m_{rn}/r\} \quad (27)$$

$$C^m_{\zeta n} = 2\Omega\{-(n+1)\,c(n,m)\,\delta^m_{n-1} - nc(n+1,m)\,\delta^m_{n+1} + im[n(n+1)]^{-1}\,\zeta^m_n + n(n+1)[-c(n,m)\,M^m_{rn-1} + c(n+1,m)\,M^m_{rn+1}]/r\}, \quad (28)$$

where the coefficient function c is defined as

$$c(n,m) = n^{-1}[(n^2-m^2)/(4n^2-1)]^{1/2}. \quad (29)$$

In the radial direction, finite differences are applied with a staggered grid. The variables p, ρ, δ, and ζ are placed on the same levels (K) while M_r is placed on interleaving levels ($K+\frac{1}{2}$, the half levels). The domain is assumed to be a spherical shell bounded between the bottom radius r_b and top radius r_t. The boundaries are chosen to be on half levels where M_r can be conveniently set to zero.

To ensure the numerical conservation of total mass and total angular momentum, the terms of Eqs. (5)–(9) involving radial derivatives can be put in a strong conservation form (expressed as derivatives with respect to r) by multiplying Eqs. (5), (6), (9) with r^2 and Eqs. (7), (8) with r^4. Furthermore, to preserve second-order accuracy of the finite-differencing in a nonuniform distribution of the radial grid points, a smooth coordinate transform can be performed between the r-space and the index space where the grid is always uniform and central differencing can be used (see the Appendix of [37]). These are in fact implemented in the code, but are not introduced in the equations shown here to avoid further complicating the notation.

Evaluation of the nonlinear terms is performed in the grid space. For this purpose, the two diagnostic variables M_θ and M_ϕ needed for Eqs. (19)–(22) are computed from the prognostic variables with the following formulas:

$$(sM_\theta)^m_n = r\{-c(n,m)\,\delta^m_{n-1} + c(n+1,m)\,\delta^m_{n+1} + im[n(n+1)]^{-1}\,\zeta^m_n\} \quad (30)$$

$$(sM_\phi)^m_n = r\{-c(n,m)\,\zeta^m_{n-1} + c(n+1,m)\,\zeta^m_{n+1} - im[n(n+1)]^{-1}\,\delta^m_n\}. \quad (31)$$

Together with the prognostic variables, these variables are transformed to the grid space with equations like Eq. (25). The grid values of V_θ and V_ϕ are then computed as M_θ/ρ_0 and M_ϕ/ρ_0, respectively.

The latitudinal locations of the grid points are determined by the roots of the Legendre function $P_{I_{\max}}(\chi)$, where $I_{\max}$ is the number of Gaussian grid points from pole to pole. The azimuthal locations of the grid points are equally spaced in ϕ; for the convenience of performing fast Fourier transforms, their total number $J_{\max}$ is chosen to be a power of two. The number of grid points is chosen to satisfy the standard requirements for unaliased transformation of quadratic nonlinearities, namely,

$$I_{\max} \geqslant (3n_{\max}+1)/2$$

and

$$J_{\max} \geqslant 3m_{\max}+1,$$

where $n_{\max}$ is the maximum degree of the spherical harmonics in the truncated expansion and $m_{\max}$ is the maximum value of m.

After the nonlinear terms are formed, three types of transform are used to evaluate them in spectral space. Let us consider an arbitrary term N. When the term involves no horizontal derivatives, an inverse Fourier transform is performed:

$$N^m_I(r_K) = (2\pi)^{-1}\sum N_{IJK}e^{-im\phi_J}, \quad (32)$$

where the sum is over J. The grid indices I, J, K are for the latitudinal, azimuthal, and radial directions, respectively. This is followed by a Gaussian quadrature

$$N^m_n(r_K) = \sum N^m_I(r_K)\,w_I P^m_n(\chi_I), \quad (33)$$

where the sum is over I, and w_I are the Gaussian weights.

When the term has a differential operator ∂_ϕ at the front, the Fourier transform is preceded by an integration by parts:

$$\int(\partial_\phi N)\,e^{-im\phi}\,d\phi = \int(imN)\,e^{-im\phi}\,d\phi. \quad (34)$$

When the term has the operator $s^{-1}\partial_\theta s$ at the front, the Gaussian integration is changed to

$$\int[s^{-1}\partial_\theta(sN)]\,P^m_n s\,d\theta = -\int N\partial_\theta P^m_n\,d\theta = -\int N(d/d\chi)\,P^m_n\,d\chi \to -\sum N^m_I(r_K)\,w_I(d/d\chi)\,P^m_n(\chi_I), \quad (35)$$

after a regular inverse Fourier transform.

As mentioned earlier, the time-implicit treatment of the linear terms is an important component of this approach. Formally, this is realized by an operator splitting technique that partitions the r.h.s. of Eqs. (5)–(9) into two implicit

steps and one explicit step [38]. For simplicity of notation, let us consider this set of equations in the form

$$\partial_t y = (W + D + C)\, y + N[y], \tag{36}$$

where y is a column array containing all the prognostic variables. Taking a finite difference in time yields the following approximation to Eq. (36):

$$(y^{q+1} - y^q)/\Delta t = \beta(W + D + C)\, y^{q+1} + (1-\beta)(W + D + C)\, y^q + N^q[y^q, y^{q-1}] + (\beta - \tfrac{1}{2})\, O(\Delta t) + O(\Delta t^2). \tag{37}$$

The superscript q is the time step index; Δt is the time step; β is a parameter describing the degree of implicitness; $\beta = 0$ and 1 correspond to the forward and backward Euler time-differencing schemes, respectively. A number of explicit methods [39] may be used for advancing the nonlinear operator N. The specific choice depends upon the accuracy requirement and efficiency consideration. Normally, a second-order method is adequate. The truncation errros associated with Eq. (37) can then be represented by its last two terms; when $\beta = \frac{1}{2}$, second-order accuracy in time can be obtained. With $\Delta y = y^{q+1} - y^q$, the equation can be rearranged as

$$[1 - \Delta t\beta(W + D + C)]\, \Delta y = \Delta t[(W + D + C)\, y + N]^q, \tag{38}$$

where the error estimates are dropped for convenience. To obtain Δy, it is necessary to invert the matrix associated with $1 - \Delta t\beta(W + D + C)$. The W and D operators couple vertical levels through ∂_r but do not couple different (n, m) modes. The matrix associated with $W + D$ is blocked tri-diagonal; the block size is 5×5. The C operator is troublesome because the Coriolis force couples the nth harmonic mode to the $n+1$ and $n-1$ modes; that would enlarge the blocks by $(n_{\max} + 1)^2$ times, and thus increase the operation counts drastically. Therefore, we split the operator with the approximation:

$$1 - \Delta t\beta(W + D + C) \approx [1 - \Delta t\beta(W + D)][1 - \Delta t\beta C]. \tag{39}$$

Then Eq. (38) can be written as

$$[1 - \Delta t\beta(W + D)][1 - \Delta t\beta C]\, \Delta y = \Delta t[(W + D + C)\, y + N]^q. \tag{40}$$

The truncation error of the approximation, Eq. (39), introduced into Eq. (40) has a formal order $O(\Delta t^3)$ and therefore second-order time accuracy can be maintained for $\beta = \frac{1}{2}$.

The solution of Eq. (40) involves three steps: (i) compute the r.h.s. explicitly; (ii) invert a block tri-diagonal matrix in the K space (the first factor on the left-hand side of the equation); (iii) invert a blocked tri-diagonal matrix in the n space (the second factor); note that the C operator does not couple harmonic components with different m values. Each element of these matrices is in fact a vector. For example, when the matrix operates on the K index (due to the ∂_r operator), all the other indices (n and m) are untouched, and they can be lumped together as the index of a long vector. This nice property is the key to vectorizing the implicit code. The procedure performed in Eq. (39) is very similar to the alternating direction implicit technique applied in regular multiple spatial dimensions [40–41]. Here, the directions are part spatial $(W + D)$ and part spectral (C), but the mathematical considerations are the same. The advantage of including the C terms in the implicit treatment will be illustrated in Section 4.

4. TESTS

A. *The Two-Dimensional Non-divergent Barotropic Case*

Using Eqs. (12), (21), and (28), the equation of motion for this highly simplified case is reduced to

$$\partial_t \zeta_n^m = 2i\Omega m[n(n+1)]^{-1}\, \zeta_n^m - [\nabla_H \cdot (\zeta \mathbf{V}_H)]_n^m. \tag{41}$$

In this situation, both the kinetic energy $\frac{1}{2}\int \mathbf{V}_H^2\, d\varpi$ and enstrophy $\frac{1}{2}\int \zeta^2\, d\varpi$ are formally conserved, even in the truncated spectral representation [34]. However, in actual numerical integration, the conservation can only be approximate, mainly due to the accumulation of truncation errors in time stepping. We test the conservation of these quantities and their dependencies on the time step size with a model on the sphere $r = 1$, truncated at $n = 4$. Initially, $\zeta_n^{\pm 1} = 1 \pm i$ for $n = 1, \ldots, 4$, and all other components are zero. The maximum velocity generated by this field is about 3.4. The evolution of the model is computed primarily by the method described in the previous section; the Coriolis term is treated implicitly with $\beta = 0.5$ and the advection term is advanced by the second-order Adams–Bashforth method [39]. For $\Omega = 1$, the time evolutions of the energy (lower curves) and enstrophy (upper curves) using time steps 0.025, 0.05, and 0.1 are shown by the solid, dashed, and dotted curves respectively in Fig. 1 (some curves overlap). Two points can be made here. First, when the time steps are small, the conservation is extremely good (even though the Adams–Bashforth method is unstable for oscillatory modes such as advected wave structures). Second, when the time steps get larger, the conservation deteriorates. This shows that time truncation errors are indeed the culprit.

We have also computed cases with $\Omega = 10$ and 100 with $\Delta t = 0.05$. These are situations where stability conditions for explicit time integrations are violated. However, in our implicit treatment, the energy and enstrophy curves even for these cases are almost identical to those that are stable (dashed curves). For comparison, the case with $\Omega = 10$ and $\Delta t = 0.05$ is also computed fully explicitly by the Adams–Bashforth method and the results are shown by the dot-dashed curves in Fig. 1. The energy and enstrophy can be seen to blow up quickly. This exercise illustrates that the stability provided by the implicit treatment of the Coriolis term helps the energy and enstrophy conservation. Being conservative does not imply that the solutions are accurate because the phase information may not be correct. But being able to use larger time steps may still be an advantage for problems that need long integration time (e.g., thermal or dynamical relaxation) and where the transients are not important.

At this point, it is useful to comment on the conservation of the total mass and total angular momentum of the full-scale model. Why can they be conserved to round-off but the energy and enstrophy here cannot? This is because in the former case each quantity involves only one spectral component (e.g., ζ_1^0 for the angular momentum). If the r.h.s. of the evolutionary equation of the integral of this component can be formally proven to be zero, then any numerical time stepping that involves a linear combination of the r.h.s. at different time levels preserves this property. On the other hand, the total energy and enstrophy are nonlinear combinations of all the components; therefore, the formal properties cannot be carried over to the numerical regime.

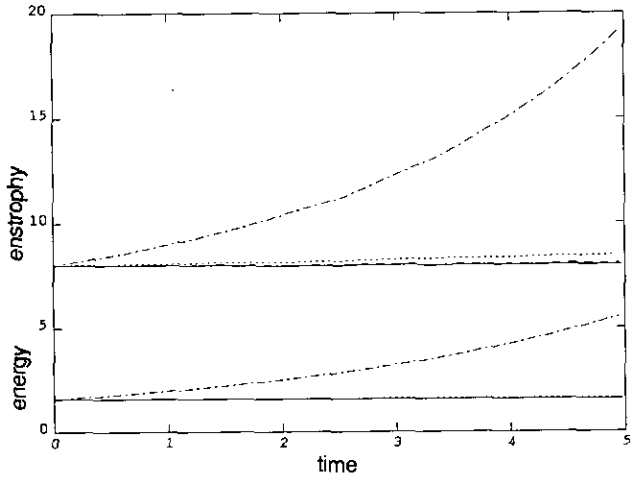

FIG. 1. Dependence of energy (lower curves) and enstrophy (upper curves) conservation on size of time steps. The solid, dashed, and dotted curves show results of implicit calculations of a case with $\Omega = 1$, using time steps 0.025, 0.05, and 0.1, respectively. The results of implicit calculations with $\Omega = 10$ and 100, using a time step of 0.05, almost coincide with the dashed curve for the $\Omega = 1$ case. A second-order explicit calculation with $\Omega = 10$, using a time step of 0.05, is unstable (the dot-dashed curves).

B. *Normal Mode Analysis*

A common test of global circulation models is to confirm that the Hough modes are indeed normal modes of the system [42]. We perform this test by looking at the solution of the linear equation,

$$i\omega y - (W + C)\, y = d, \tag{42}$$

where d is a driver that excites the system. This equation comes from Eq. (36) with the viscosity, diffusion, and nonlinear terms dropped. The temporal variation of the solution and the driver has been taken to be $e^{i\omega t}$ so that the time derivative becomes a multiplicative factor $i\omega$. Here, we concentrate on cases with $\omega = \Omega$ (diurnal tide) for which the spectral expansions of the Hough modes are well documented [43–44]. When the driver d has the form of a particular Hough mode, the solution y should come out to be proportional to that same mode if the Hough mode is indeed a normal mode of the system.

Since the thin-shell approximation is usually adopted in the derivation of the Hough modes, we perform the test by setting up a stable background atmosphere in a very thin layer (1% of the radius). The distribution is polytropic (i.e., the pressure is a power function of density; see next subsection), but the details are not important for the Hough modes. Figure 2 shows the latitudinal pressure distributions of some Hough modes (solid curves) used to drive the system and the responses (marked by the x symbols). The identifications of the modes are labeled next to the curves (adopting the notations of [43]). The results demonstrate that the Hough modes are indeed normal modes of the system. For comparison, a driver that is not a Hough mode (dashed curve) yields a response (dot-dashed curve) that is very different.

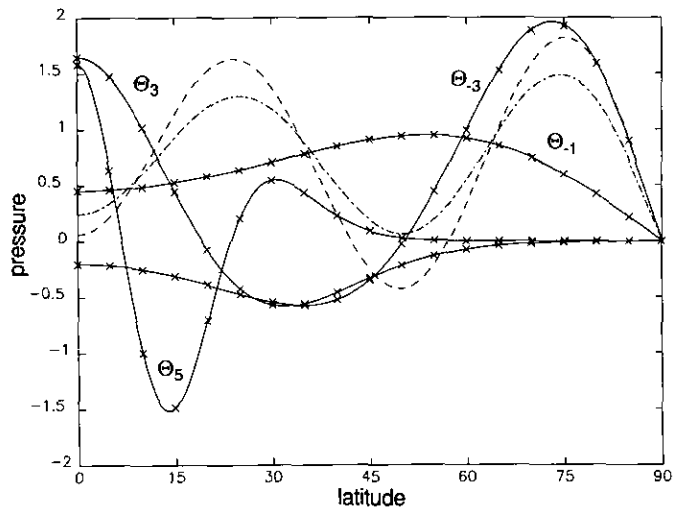

FIG. 2. Linear responses of the model (pressure versus latitude) driven by Hough functions (solid curves) and a non-Hough function (dashed curve). The response to a Hough mode is represented by the × signs and to the non-Hough mode by the dot-dashed curve.

C. *Onset of Convection in an Axisymmetric Hemispheric Shell*

Computing the onset of convection offers a very sensitive test of the subtle balances of all the linear terms and demonstrates the capability of the model to handle convection. The stratified spectral model is used to find the critical Rayleigh numbers for a series of parameters, and the results are compared to those obtained by a finite-difference model solving the complete set of Navier–Stokes equations [45, 35]. The test problem is specified as follows: (i) The region is an axisymmetric hemispheric shell with top boundary at $r_t = 1$ and bottom boundary at $r_b = 0.5$. (ii) The gravitational acceleration g is taken to be inversely proportional to r^2. (iii) The fluid is an ideal gas with constant dynamic viscosity μ and conductivity κ; $\lambda = -\frac{2}{3}\mu$. The Prandtl number Pr and the ratio of specific heats γ are chosen to be 1 and $\frac{5}{3}$, respectively. (iv) The initial distribution is polytropic ($p \propto \rho^{1+1/n_p}$) and in hydrostatic and radiative equilibrium ($\mathbf{f} = -\kappa\nabla T$),

$$T/T_t = \psi = 1 + Z(r_t/r - 1)/(r_t/r_b - 1) \tag{43}$$

$$\rho/\rho_t = \psi^{n_p} \tag{44}$$

$$p/p_t = \psi^{n_p+1}, \tag{45}$$

where the subscripts b and t denote values at bottom and top, respectively. The parameter $Z = T_b/T_t - 1$ describes the depth of stratification. If the polytropic index n_p is smaller than $1/(\gamma - 1)$ (i.e., 1.5), the layer is convectively unstable; otherwise, it is stable. In the present case, Z and n_p are chosen to be 1 and 1.4, respectively. Hereafter, the values of all the quantities will be expressed in units which make r_t, ρ_t, p_t, $T_t = 1$. (v) The boundaries are stress-free and the temperatures at the top and bottom are fixed at the initial values. The Rayleigh number is defined as [46]

$$\mathrm{Ra} = \mathrm{Pr}\, gZ(r_t - r_b)^3\,(1 - (\gamma - 1)\, n_p)\, \rho_t^2/(\gamma\mu^2). \tag{46}$$

As an initial perturbation, a very small vertical velocity field is introduced to the fluid, and its evolution is computed to determine whether the perturbation is growing or decaying. After a few trials, one can find the critical Rayleigh number above which convection starts. The spectral model has 41 vertical grid points and $n_{\max} = 30$. The finite-difference model has the same number of vertical grid points and the number of horizontal grid points is 61. However, the latter does not reach the pole; its pole-side boundary is at 1.5° colatitude. A comparison of the critical Rayleigh numbers Ra_c for a number of Ω (in units defined above) is given in Fig. 3, where $\log_{10}(\mathrm{Ra}_c)$ are plotted versus $\log_{10}(\mathrm{Ta})$. The Taylor number, Ta, is defined as

$$\mathrm{Ta} = 4\Omega^2(r_t - r_b)^4\,(\rho_t/\mu)^2. \tag{47}$$

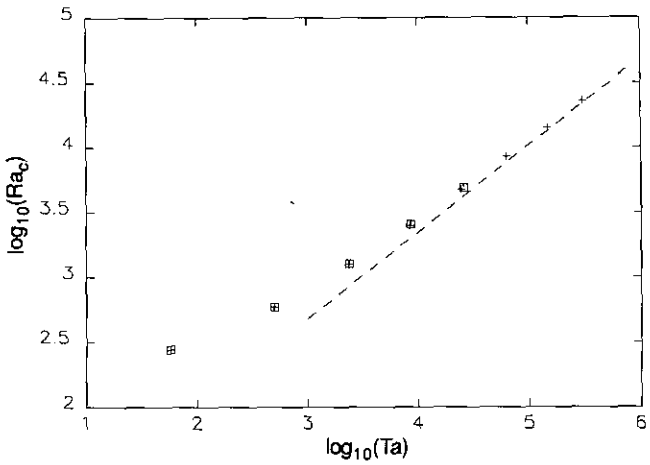

FIG. 3. Comparison of critical Rayleigh numbers obtained by the spectral code (the pluses) and the finite-difference code (squares) for $\Omega = 0.1$, 0.2, 0.3, 0.4, and 0.5. As the rotation rate increases ($\Omega = 0.6$, 0.7, and 0.8), the critical Rayleigh number demonstrates an asymptotic dependence on the Taylor number, namely, $\mathrm{Ra} \propto \mathrm{Ta}^{2/3}$. The dashed line shows the $\frac{2}{3}$ slope in the log–log plot.

The pluses and squares stand for the results of the spectral and finite-difference models, respectively. In all the cases, the differences are less than 4%. Considering the slight difference in geometrical configurations and the influences of the truncation errors, the agreement is very good.

An interesting feature revealed by Fig. 3 is the growth of the critical Rayleigh number with the rotation rate, showing that rotation hinders convection. We pursued this phenomenon further using the spectral code to find the critical Rayleigh numbers for a few higher rotation rates. The dashed line in Fig. 3 displays a slope of $\frac{2}{3}$ which is the asymptotic ($\mathrm{Ta} \to \infty$) power dependence of Ra_c on Ta derived for an incompressible fluid [47]. Apparently, this behavior also occurs for the compressible fluid. To facilitate future comparison, we list the values of Ra_c for these cases in Table I.

TABLE I

Critical Rayleigh Numbers for Different Rotation Rates

Ω	Ra_c
0.0	1.99×10^2
0.1	2.78×10^2
0.2	5.90×10^2
0.3	1.25×10^3
0.4	2.50×10^3
0.5	4.72×10^3
0.6	8.42×10^3
0.7	1.42×10^4
0.8	2.27×10^4

D. *Finite-Amplitude Convection in an Axisymmetric Hemispheric Shell*

The computation of finite amplitude, stationary convection provides a sensitive test of the interplay of linear and nonlinear terms. Also, by comparing the results of the spectral model using the stratified approximation with those of the complete Navier–Stokes equations, one can assess the magnitude of errors introduced by the approximation. The test problem is similar to the one used in the previous subsection, with the following differences: (i) The lower boundary is at $r_b = 0.7$. (ii) The rotation rate is zero. The parameter Z remains one. (iii) The number of vertical grid points is 30. The finite-difference code uses 80 horizontal grid points between the equator and the north pole. The spectral code uses 40 spherical harmonics, but also uses 80 latitudinal points in real space for easy comparison with the finite-difference results. The pole-side boundary of the finite-difference model is at 1.2° colatitude. (iv) The flows are initiated with rolls symmetric with respect to the equator, and the vertical velocities at the poles are downward.

The maximum horizontal (diamonds for spectral, pluses for finite-difference) and vertical (triangles for spectral, stars for finite-difference) velocities in the flows are plotted in Fig. 4 for several supercritical Rayleigh numbers ($\mathrm{Ra}_c = 250$), and the maximum Mach numbers attained by the flows are listed in Table II (note that maximum velocity and maximum Mach number need not occur at the same location). As shown in Fig. 4, the agreements between the results of the two codes are quite good. In accord with expectation, discrepancies increase with the Mach number as the errors introduced by the stratified approximation become larger. In the most vigorous case here (the rightmost points), the Mach number reaches about 0.15 and the maximum difference is about 2%. Both codes show that a transition in flow pattern occurs between the Rayleigh numbers 1000 and 2000 (from three cells to two cells between the pole and equator); V_r remains negative at the poles in all cases.

TABLE II

Maximal Mach Numbers for Different Rayleigh Numbers

Ra	Mach number	No. of cells
300	0.046	3
500	0.082	3
1000	0.105	3
2000	0.133	2
3000	0.144	2
4000	0.153	2

Comparison of the transients to a steady state as computed by different time steps shows how the efficiency of the semi-implicit spectral method can be exploited. In Fig. 5, this is done with the $\mathrm{Ra} = 300$ case. The dots, pluses, and stars represent every 10 steps of computations with $\Delta t = 0.04$, 0.4, and 4, respectively, corresponding to sound speed CFL numbers about 5, 50, and 500, respectively. The transients agree well, showing that even rather large time steps do not destroy the time accuracy of the computation.

5. SUMMARY

In this paper, a non-hydrostatic spectral model applicable to both convective and stable atmospheres is presented. Even though the hydrostatic approximation is eliminated, the model is able to use large time steps, taking advantage of the simplicity of implementing the semi-implicit time

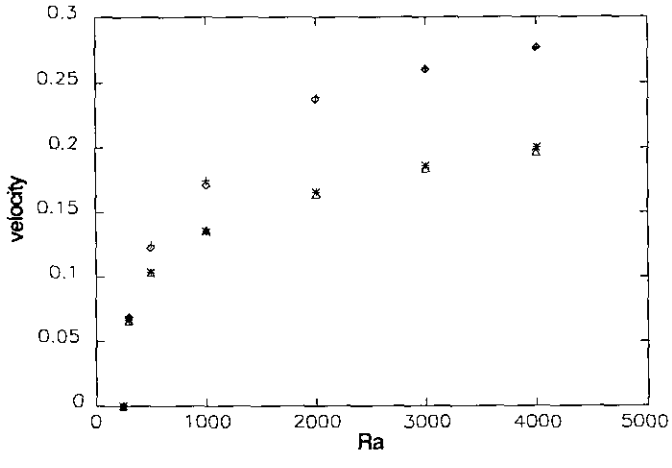

FIG. 4. Maximum vertical and horizontal velocities computed by the finite-difference and spectral codes. The symbols for the velocities are: pluses (finite-difference, horizontal), diamonds (spectral, horizontal), stars (finite-difference, vertical), and triangles (spectral, vertical). Discrepancies increase with the Mach number (see Table II).

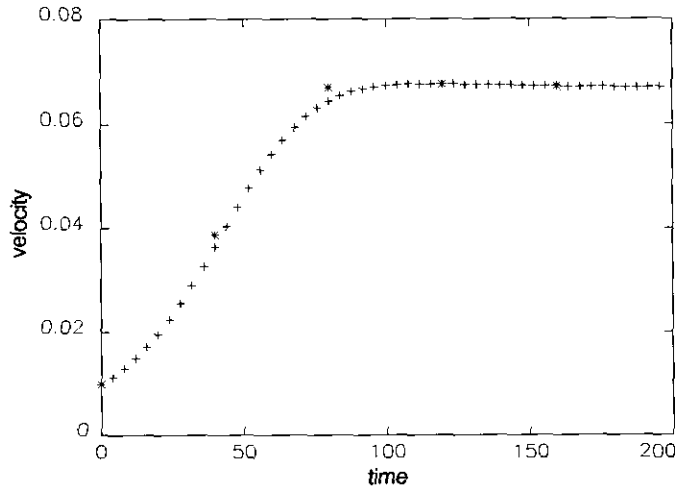

FIG. 5. Comparison of transients of relaxation to a steady state, all computed with the implicit method. The sound speed CFL numbers for the dots, pluses, and stars are 5, 50, and 500, respectively.

integration in a spectral approach. Essentially all of the linear terms that appear in the Navier–Stokes equations remain intact; therefore all the waves generated by these terms can be exactly described (the acoustic waves are important, for example, to the study of helioseismology [48]). The advantage of this approach over the anelastic approach is summarized in the Appendix. The relative increase in computational load is quite insignificant for moderate or large size problems in which the spectral transforms are the dominant part of the calculation.

The *stratified approximation* is introduced to make the nonlinear terms quadratic in the harmonic expansion so that alias-free transformations can be easily implemented, and to simplify the derivation of the prognostic equations so that they can be put in simple closed forms similar to those derived for the hydrostatic models. De-aliasing has several advantages. First, it maintains total mass conservation and total angular momentum conservation both formally and numerically. Second, it does not break the symmetry of a flow (e.g., equatorial symmetry) unnecessarily. Third, it enhances numerical stability. The price to pay—assuming that the horizontal variations of the thermodynamic variables are small—is quite insignificant for normal atmospheric conditions (see the Appendix). In contrast with aliasing errors, the errors introduced by the stratified approximation are associated with a physical approximation and can be estimated as such; they do not intrinsically lead to numerical instabilities.

The numerical efficiency and the conservation properties of the present model make it particularly suitable for studies involving long-period integration. Examples include self-consistent thermal and dynamical relaxation of an atmosphere, generation of prevailing circulations, and climatic studies. The scale of vectorization of the model is competitive with finite-difference, explicit codes; the sustained rate of computation easily reaches 110 Mflops in one processor of a Cray Y-MP. In an application to compute Earth's diurnal tides (from surface to 600 km altitude, 226 vertical levels, $n_{\max} = 10$, $m_{\max} = 1$), it takes 16 min in a Micro-Vax 3100-80 machine to compute one day of evolution (with 15 min time steps).

Some atmospheric studies require the computation of small scale phenomena, e.g., gravity wave breaking. In such cases, a Cartesian configuration is more convenient. However, the curl-divergence formulation and the stratified approximation developed here still offer much computational advantage and can be easily implemented.

An axisymmetric version of the present model has been used to study the spin up of the 4-day superrotation of the Venusian atmosphere via the Hadley mechanism and a linear version which couples the C-terms and the W-terms in a single matrix has been applied to study the internal rotation of the solar convection zone. Details of these applications will be presented in later papers.

APPENDIX: CONTRASTING THE STRATIFIED AND ANELASTIC APPROXIMATIONS

Since both assume that the horizontal variations of the thermodynamic variables are small, the stratified and the anelastic approximations have some similarities. The principal difference is that the stratified approximation does not make this assumption for the linear terms of Eqs. (2)–(4). In some situations (e.g., a stationary mean circulation driven by differential heating in a stable atmosphere), the horizontal variations of the thermodynamic variables are proportional to the flow speed and thus of first order in the Mach number (the circulation is essentially a particular solution of the linear part of the hydrodynamic equations plus an external driver). Since the stratified approximation eliminates second and higher order products of such variations *only* in the advection terms which already contain a velocity factor, a formal accuracy of second order in the Mach number is still guaranteed for this approximation, but not for the anelastic approximation. In time-dependent, significantly nonlinear situations, the relative fluctuations of the thermodynamic variables are proportional to the square of the Mach number [35] (see also later discussion). Since acoustic waves are in fact present, the relative error introduced through neglecting $\partial_t \rho$ in the continuity equation should be estimated as $\partial_t \rho / (\rho \nabla \cdot \mathbf{V}) \sim \omega \rho_1 / (\rho_0 k v)$, where ω, k, and v are certain characteristic frequency, wave number, and velocity, respectively. Using the dispersion relationship $v_s = \omega / k$ for acoustic waves (v_s is the sound speed), the above ratio can be written as $(\rho_1/\rho_0)(v_s/v) \sim (v/v_s) \sim$ the Mach number. It is therefore more substantial than the errors introduced by neglecting perturbations like $(\rho_1/\rho_0)^2 \cdots$.

To further illustrate the advantage of solving for the density variation through the continuity equation directly, we demonstrate the last point made in the above paragraph with a numerical example which solves the fully compressible Navier–Stokes equations. This example is based on a recent study of deep convection made by Chan and Gigas [49], and the code is the Cartesian version of the finite-difference code used for the calculations described in Sections 4C and D. The physical parameters and configuration of the calculation described here are the same as those in [49]; the only difference is the enhanced vertical resolution used here. The salient features of the calculation are: (i) The Navier–Stokes equations are solved for an ideal gas in a three-dimensional rectangular domain; the mesh contains $69 \times 69 \times 100$ points. (ii) The upper and lower boundaries are stress-free and impenetrable; the side boundaries are periodic. The temperature at the top is held fixed; a constant input flux is imposed at the bottom. (iii) The gas consists of three layers; one thick convective layer lies between two thinner stable layers whose main function is to separate the convection from the upper and lower boundaries. The for-

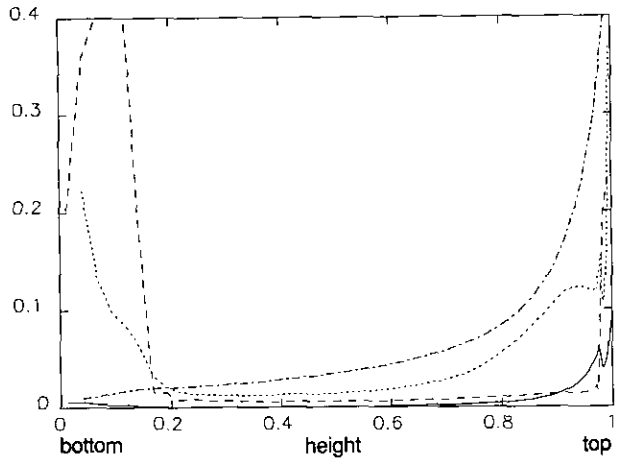

FIG. 6. Distributions of relative fluctuations in a convection zone bounded by upper and lower stable layers. The boundaries between the convection zone and the stable layers can be identified by the locations (heights ~ 0.17 and 0.98) where the radiative flux (dashed curve) exhibits jumps from near zero to large values. The r.m.s. Mach number is represented by the dot-dashed curve. The ratios r.m.s.$\{\nabla\cdot(\rho\mathbf{V})\}$/r.m.s.$\{\rho\nabla\cdot\mathbf{V}\}$ and r.m.s.$\{\rho_1\}/\rho_0$ are shown by the dotted and solid curves, respectively.

mation of these layers is achieved by controlling the height dependence of the conductivity. In the convective layer, the conductivity is set to low values, so that more than 90% of the energy flux is carried by convection. (iv) Statistical information on the fluctuating quantities are obtained through horizontal and temporal averaging after the fluid arrives at statistical thermal and dynamical equilibrium.

Figure 6 shows the distribution of several quantities relevant to our present interest. All quantities are expressed in units which set the total depth and the initial pressure, temperature, and density at the top to one. In such units, the total energy flux flowing through the layer has a value of 0.25. The dash curve shows the distribution of the conductive flux which stays low in the convective region, and the boundaries between the convective and stable regions are marked by the jumps in this flux. The Mach number is represented by the dot-dashed curve. The root-mean-square (r.m.s.) of $\partial_t\rho$ is compared with r.m.s.$\{\rho\nabla\cdot\mathbf{V}\}$ and shown as a ratio by the dotted curve. This curve parallels that of the Mach number and reaches above 10% at the upper region of the convection zone where the Mach number is ~ 0.2. (Near the top and bottom boundaries, the dotted curve shoots up as the upward and downward directing flows impinge on the impenetrable boundaries.) Therefore the ratio is of first order in the Mach number as suggested by the previous scale analysis. In comparison, the relative fluctuation of density, r.m.s.$\{\rho_1\}/\rho_0$, shown by the solid curve is significantly smaller and is of second order in the Mach number. Other thermodynamic variables, although not shown here, have similar behavior.

ACKNOWLEDGMENTS

We thank J. R. Bates, W. C. Chao, and J. E. Nielsen, M. Fox-Rabinowitz, M. J. Suares, and R. F. Theis for discussions and comments. K.L.C. thanks NSF for support (ATM-9108315) and the Pittsburgh Supercomputing Center for providing computer time.

REFERENCES

1. G. Schubert, C. Covey, A. Del Genio, L. S. Elson, G. Keating, A. Seiff, R. E. Young, J. Apt, C. C. Counselman III, A. J. Kliore, S. S. Limaye, H. E. Revercomb, L. A. Sromovsky, V. E. Suomi, F. Taylor, R. Woo, and U. Von Zahn, *J. Geophys. Res.* **85**, 8007 (1980).
2. R. F. Beebe, A. P. Ingersoll, G. E. Hunt, J. L. Mitchell, and J.-P. Muller, *Geophys. Res. Lett.* **7**, 1 (1980).
3. S. S. Limaye, H. E. Revercomb, L. A. Sromovsky, R.-J. Krauss, D. A. Santek, and V. E. Suomi, *J. Atmos. Sci.* **39**, 1413 (1982).
4. H. B. Hammel, R. F. Beebe, E. M. De Jong, C. J. Hansen, C. D. Howell, A. P. Ingersoll, T. V. Johnson, S. S. Limaye, J. A. Magalhaes, J. B. Pollack, L. A. Sromovsky, V. E. Suomi, and C. E. Swift, *Science* **245**, 1367 (1989).
5. H. W. Newton and M. L. Nunn, *Mon. Not. Roy. Astron. Soc.* **111**, 413 (1951).
6. H. G. Mayer, K. L. Chan, I. Harris, and K. Schatten, *Astrophys. J.* **367**, 361 (1991).
7. T. B. Brown, J. Christensen-Dalsgaard, W. A. Dziembowski, P. Goode, D. O. Gough, and C. Morrow, *Astrophys. J.* **343**, 526 (1989).
8. K. G. Libbrecht, *Astrophys. J.* **336**, 1092 (1989).
9. K. L. Chan and K. Serizawa, "On Numerical Studies of Solar/Stellar Convection," in "The Sun and Cool Stars: Activities, Magnetism, Dynamos" edited by I. Tuominen, D. Moss, and G. Rudiger (Springer-Verlag, Berlin, 1991), p. 15.
10. S. A. Orszag, *J. Atmos. Sci.* **27**, 890 (1970).
11. E. Eliasen, B. Machenhauer, and E. Rasmusen, University of Copenhagen Rep. No. 2, Institute for Theoretical Meteorology, Copenhagen, 1970.
12. I. Silberman, *J. Meteor.* **11**, 27 (1954).
13. S. Kubota, *Pap. Meteor. Geophys. (Tokyo)* **10**, 145 (1959).
14. H. W. Ellsaesser, *J. Appl. Meteor.* **5**, 246 (1966).
15. A. J. Robert, *J. Meteor. Soc. Jpn* **44**, 237 (1966).
16. W. Bourke, *Mon. Wea. Rev.* **102**, 687 (1974).
17. B. J. Hoskins and A. J. Simmons, *Quart. J. R. Met. Soc.* **101**, 637 (1975).
18. R. Daley, C. Girard, J. Henderson, and I. Simmonds, *Atmosphere* **14**, 98 (1976).
19. J. G. Sela, *Mon. Wea. Rev.* **108**, 1279 (1980).
20. C. T. Gordon and W. F. Stern, *Mon. Wea. Rev.* **110**, 625 (1982).
21. M. Kanamitsu, K. Tada, T. Kudo, N. Sata, and S. Isa, *J. Meteorol. Soc. Jpn* **61**, 812 (1983).
22. S. Manabe, D. G. Hahn, and J. L. Holloway, *Climate Simulation with GFDL Spectral Models of the Atmosphere: Effect of Spectral Truncation*, GARP Publ. Ser., No. 22 (GARP, Geneva, 1979), p. 41.
23. C. Girard and M. Jarraud, ECMWF Technical Report No. 32, 1982, p. 178 (unpublished).
24. A. J. Robert, in *Proceedings, WMO/IUGG Symposium on Numerical Weather Prediction, VII*, p. 19, Japan Meteor. Agency, Tokyo, 1969.
25. A. J. Simmons, B. J. Hoskins, and D. M. Burridge, *Mon. Wea. Rev.* **106**, 405 (1978).
26. Y. Ogura and J. G. Charney, in *Proceedings, Intern. Symp. Num. Wea. Prediction, Tokyo, 1962*, p. 431.
27. Y. Ogura and N. A. Phillips, *J. Atmos. Sci.* **19**, 173 (1962).

28. D. O. Gough, *J. Atmos. Sci.* **26**, 448 (1969).
29. R. E. Young and J. B. Pollack, *J. Atmos. Sci.* **34**, 1315 (1977).
30. G. A. Glatzmaier, *J. Comput. Phys.* **55**, 461 (1984).
31. G. I. Marchuk, WMO Tech. Note No. 66, p. 286 (1965).
32. M. Tanguay, A. Robert, and R. Laprise, *Mon. Wea. Rev.* **118**, 1970 (1990).
33. G. W. Platzman, *J. Meteor.* **17**, 635 (1960).
34. B. Machenhauer, *The Spectral Method*, GARP Publ. Ser., No. 17, II (GARP, Geneva, 1979), p. 121.
35. K. L. Chan and S. Sofia, *Astrophys. J.* **336**, 1022 (1989).
36. J. P. Cox and R. T. Giuli, *Principles of Stellar Structure* (Gordon & Breach, New York, 1968).
37. K. L. Chan and S. Sofia, *Astrophys. J.* **307**, 222 (1986).
38. N. N. Yanenko, *The Method of Fractional Steps* (Springer-Verlag, New York, 1971).
39. C. W. Gear, *Numerical Initial Value Problems in Ordinary Differential Equations* (Prentice-Hall, Englewood, NJ, 1971).
40. D. W. Peaceman and H. H. Rachford, Jr., *J. Soc. Indust. Appl. Math.* **3**, 28 (1955).
41. J. Douglas, Jr., *J. Soc. Indust. Appl. Math.* **3**, 42 (1955).
42. W. C. Chao and M. A. Geller, *Mon. Weather Rev.* **110**, 304 (1982).
43. R. S. Lindzen, *Mon. Weather Rev.* **94**, 295 (1966).
44. S. Chapman and R. S. Lindzen, *Atmospheric Tides—Thermal and Gravitational* (Gordon & Breach, New York, 1970).
45. K. L. Chan and C. L. Wolff, *J. Comput. Phys.* **47**, 109 (1972).
46. E. Graham, *J. Fluid Mech.* **70**, 689 (1975).
47. S. Chandrasekhar, *Hydrodynamic and Hydromagnetic Stability*, (Oxford Univ. Press, Oxford, 1961).
48. A. N. Cox, S. M. Chitre, S. Frandsen, and P. Kumar, "Oscillation Mode Excitation," in *Solar Interior and Atmosphere*, edited by A. N. Cox, W. C. Livingston, and M. S. Matthews (Univ. of Arizona Press, Tucson, 1991), p. 618.
49. K. L. Chan and D. Gigas, *Astrophys. J. (Lett.)* **389**, L87 (1992).